Distributed Nonlinear Model and Fast Analysis for In-Band IMD3 Prediction of Surface Acoustic Wave Resonators

Marta González-Rodríguez, *Student Member, IEEE,* Carlos Collado, *Senior Member, IEEE,* Jordi Mateu, *Senior Member, IEEE,* José M. González-Arbesú, Sebastian Huebner, *Member, IEEE*

Abstract— The motivation of this work is to analyze the in-band intermodulation distortion (IMD) occurring in Surface Acoustic Wave (SAW) devices, using a recently developed fast method based on the Input-Output Equivalent Sources (IOES). The method calculates the equivalent current sources of a given harmonic (H) or IMD, which when applied at the boundaries of any uniform nonlinear region produce the same nonlinearities than the full distributed circuit. The accuracy of the method is validated with a very simplified SAW resonator with ten digits, which is modelled by a discretized Mason-based circuit. The IOES method provides equal results than the ones obtained through Harmonic Balance (HB) simulations, performed by means of a commercial software, being the first 1000 times faster.

Once the accuracy of the method is guaranteed, it is used to analyze the measured in-band IMD3 of several Lithium Tantalite 42º cut LSAW resonators with different pitch and duty factor at the B66 LTE frequency band. Those resonators are comprised of 100 and 20 electrode pairs for the active region and each of the reflectors respectively, which implies the analysis of a very large distributed nonlinear problem with thousands of nonlinear local sources. The IOES method takes 35.4 seconds in simulating 51 frequency points, whereas this simulation is not possible using a commercial HB simulator on a general-purpose computer.

Index Terms— Nonlinearities, SAW, electro-acoustic, harmonic distortion, intermodulation distortion, third order intermodulation product, input-output equivalent sources.

I. INTRODUCTION

With the upcoming 5th Generation (5G), manufacturers are moving towards the integration of complex multisystem RF modules, adding more intricacy to the already complicated RF front-ends. In the filter domain, the SAW/BAW technology legacy will remain stable since those very small filters are frequently used in wireless devices to meet the requirements of low insertion loss and good out-of-band rejection.

One of the most important subjects on the development of SAW/BAW devices in RF front-end is their high linearization demands. For instance, in a duplexer scenario where two SAW filters (transmitter and receiver) are combined at a common antenna, desensitization of the receiver might occur due to the generation of spurious signals caused by the nonlinearity of these passive components.

This concern led to extend the research on modeling and simulation of the nonlinearities of SAW devices during the last two decades [1]-[11]. These references used different approaches, for example, based on finite element model (FEM) [1], circuit-level design techniques [2], [3], Coupling of Modes (COM) theory [4]-[8] or P-Matrix [9]-[11]. Despite of the different published approaches, there is still a lack of generalized consensus about the origin of the nonlinear behaviour. References [12]- [14] state that the nonlinearities are given by nonlinear elasticity, dielectric constant and electromechanical coupling, [18] studies the nonlinearities arisen from the electrode crystallinity, and [15]- [17] aim to the bulk modes. The lack of consensus is driven by the difficulty to identify geometry-independent material parameters that could predict the nonlinear behaviour of any resonator before manufacturing. One reason might be the distributed nature of the nonlinearities in acoustic devices.

It has been demonstrated that distributed circuit models are particularly useful to find the nonlinear material parameters that characterize the nonlinearities of BAW resonators [19]-[22] according with well-known piezoelectric constitutive equations. Distributed models are required to reproduce the standing wave pattern of the fields along the structure at a given frequency, since the nonlinear effects arise locally at any position of the structure depending of those field magnitudes. Sweeping the frequency of the excitation, each potential contributor (source of nonlinearity) causes a characteristic frequency pattern, which enables to discern between them [20]. This characterization process allows to find the geometry-independent nonlinear parameters, which only depend on the physical properties of the materials, contributing to the generation of a given spurious signal.

Unfortunately, the main drawback of the distributed approaches is that the number of nonlinear unit-cells to analyze can be considerable large increasing dramatically the computing time. While a solidly mounted resonator (SMR)

M. González-Rodríguez, C. Collado, J. Mateu and J.M. González-Arbesú, are with the Signal Theory and Communications (TSC) Dept. from Universitat Politècnica de Catalunya (UPC), Barcelona 08034, Spain (e-mail: marta.gonzalez.rodriguez@upc.edu

S. Huebner is with Qorvo Munich, 81829 Munich, Germany.

BAW resonator is formed by 100 to 400 unit-cells [23],[24] -at least ten unit-cells per wavelength along the whole stack of materials- and distributed models can be analyzed by conventional HB simulations, the nonlinear analysis of a "discretized" SAW resonator is not a trivial task. A SAW resonator might be comprised by two hundred of digits, and therefore the total electrical length into the propagating direction could be one hundred wavelengths. Simulating several thousands of nonlinear unit-cells using commercial simulators is a very time-consuming task and might be even unfeasible.

The objective of this paper is developing a characterization process for SAW resonators to find the nonlinear parameters, which allows to predict the behavior of new devices with other in-plane geometries. To be successful in this process there are three key aspects that are tackled in this proposed technique:

1) The model must be distributed and directly related to local nonlinear constitutive equations commonly accepted by the scientific community.

2) The solution (nonlinear parameters) must be unique and able to explain the nonlinearities of resonators with different shape. Then, this parameter (or parameters) can be used for predicting the nonlinear behavior of new resonators and filters using the same materials before manufacturing. Specifically, the in-band IMD3 response is analyzed.

3) The method used to solve the problem must be rigorous, fast and applicable to solve more complicated circuits like filters or duplexers.

The model we will use is a distributed implementation of the well-known cross-field Mason model, which is directly related to the local constitutive equations of the piezoelectricity. Despite of its simplicity, it will be demonstrated that it is extremely consistent to simulate the in-band third order intermodulation of different resonators using only a geometry-independent nonlinear parameter.

Beyond the equivalent circuit, the main contribution of this work is the method we have developed to solve the circuit. According to the Thevenin and Norton theorems, any n-port circuit with many internal linear voltages or current source has an equivalent circuit with n-ports and n-sources. The method we describe in this article allows to find the equivalent current sources that placed at the boundary nodes of a given network with many internal sources provide the same results. Reference [25] describes the application of this new method to analyze BAW resonators and filters, referred as Input-Output Equivalent Sources (IOES) method, which allows to perform extremely fast and robust simulations of large distributed weakly nonlinear circuits. The application of the IOES method to SAW resonators was initially introduced in [26]. In comparison with this previous publication, here we include all the specific details of the IOES method to be applied to SAW resonators with details of all the frequency-domain equations involved to evaluate the distributed model at each frequency of interest, including indirect effects. We have also included the nonlinear analysis of the reflectors and finally, the characterization process considering simulations and measurements of many resonators having different duty factors

and pitches is discussed here for the first time.

To the best of our knowledge, this method is the only feasible method for the analysis of weak nonlinearities in SAW resonators without losing the full distributed nature of the problem with several distributed nonlinear sources per wavelength.

The document is organized as follows. Section II recalls for the distributed problem and the implementation of the model of a SAW resonator. It describes the equivalent circuit of a λ-section, which in our case refers to a one period of the interdigital electrodes, to consider later the whole transducer. Section III details the application of the IOES method to the analysis of SAW resonators. The swiftness of the proposed method is compared with HB simulations and useful considerations are discussed, such as the minimum number of discretization cells to guarantee confident results. Finally, Section IV describes the linear and nonlinear characterization process and shows examples of IMD3 measurements of different SAW resonators. It discusses about the potential contributing materials on the generations of the in-band IMD3 and it demonstrates that all the in-band IMD3 measurements close to resonance can be explained by only one geometry-independent nonlinear parameter, the third order derivative of the elastic constant.

II. DISTRIBUTED NONLINEAR MODEL ANALYSIS

A. Distributed linear model

A linear distributed model must be used, whose accuracy to emulate the linear measurements entails a proper modelling of the nonlinearities.

We assume that the main driver of the surface wave generation is the transversal electric field beneath the electrodes. Following that, and as it was done in [26], we use the crossed-field Mason circuit approach [27]. In this model, the electric field distribution under the electrodes is approximated as being constant and it mainly generates Rayleigh waves in a direction perpendicular to the electric field [28].

The conventional crossed-field model is not discretized and there is a Mason equivalent circuit for each period of the structure, that is, for each pair of digits of the inter-digital transducer (IDT) [29],[30]. We have modified this model separating the metallized regions (MR) and the non-metallized regions (NMR) of the $\lambda/2$-section as seen into the dashed box of the IDT in Fig. 1 (b). Doing so, a $\lambda/2$-section of the IDT is made up by three sub-circuits: a crossed-field Mason-based circuit for the MR section representing the area beneath the electrodes that is ended on each acoustic side by a NMR section (T-circuit) where only acoustic propagation is considered. For the reflectors, only acoustic propagation is considered along the electrode section and thus, each $\lambda/2$-section is composed by three cascaded T-networks with differentiation between NMR and MR regions as depicted in Fig. 1(b).
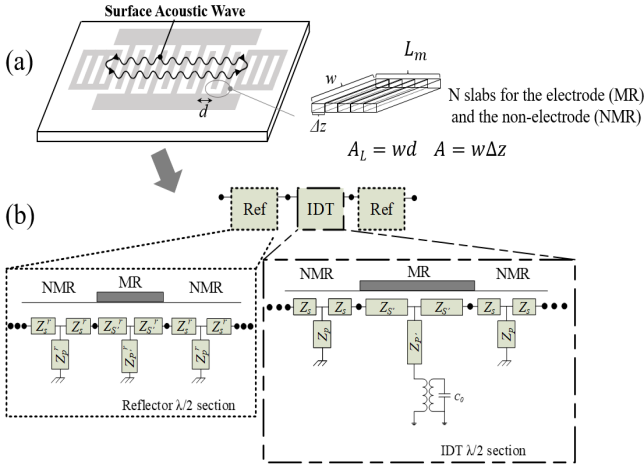
Fig. 1. (a) Example SAW device with each digit subdivided into slabs of thickness Δz. (b) Analysis model using the crossed-field approximation [26], [29].

Each MR or NMR section, whether of the IDT or acoustic reflectors, has its own acoustic impedance and phase velocity. The circuit parameters of the T-circuits modeling the acoustic propagation are described by series (Z_s) and shunt impedances (Z_p):

$$Z_s = Z_{0,m} \tanh\left(\gamma_m \frac{L_m}{2}\right) \qquad (1)$$

$$Z_p = Z_{0,m} / \sinh(\gamma_m L_m) \qquad (2)$$

where the subscript m indicates the region MR or NMR, L_m is the width of the section, $\gamma_m = \alpha_m + j\,^\omega\!/_{v_m}$ is the propagation constant and $Z_{0,m} = \rho_m A_L v_m$ is the characteristic impedance, being ρ_m and A_L the mass density and lateral area (see Fig. 1a). Although there are different phase velocities v_m for the MR and NMR of the IDT and reflector, only very small relative variations are needed. Such differentiation between IDT and reflector circuit parameters is required to model most of the features of the linear response. It will be further discussed in Section IV. The transformer ratio T and C_0 capacitance of the cross-field model of Fig. 1b are given by $T = -e \cdot w$ and $C_0 = \varepsilon_{r,eff} \cdot \varepsilon_0 \cdot A/d$ respectively. The values of the relative dielectric constant $\varepsilon_{r,eff}$ must be considered as effective values because it must be fine-tuned to adjust the linear simulations of this simplified model to the measurements as it will be discussed in section IV.B. Therefore, and besides the geometrical parameters: aperture (w), pitch (d) and duty factor, the lineal model is fully described by means of the mass density, effective dielectric constant, piezoelectric constant, and acoustic wave velocities of the MR and NMR regions.

The distributed model consists of discretizing into unit-cells each section of the MR and the NMR as depicted in Fig. 1(b). The MR will be modelled cascading many unit-cells of the crossed-field Mason circuit, each one modelling a thin slab of width Δz, where the wave propagates along the z-direction beneath the electrodes, until reaching the NMR, which is modelled cascading unit-cells of acoustic transmission lines of length Δz (see Fig.1).

Obviously, the discretized model must provide identical linear response as the non-discretized one. However, it allows

to apply locally the nonlinear constitutive equations of the piezoelectricity with parameters that are independent of the in-plane geometry (shape) of the IDT's and reflectors.

B. Distributed nonlinear model

The nonlinear unit-cells representing a MR and a NMR section are presented in Fig. 2 and Fig. 3 respectively. These unit-cells are cascaded to form the circuit of a period (λ-section), as it is illustrated in Fig. 4(b) and Fig. 4(c), and finally, the schematic for the whole transducer composed of M λ-sections and reflectors is outlined in Fig. 4(a).

The nonlinear circuit model is based on the one used in [19]-[21]. Those references were based in the so-called in-line Mason model, in which the acoustic wave propagates in the same direction than the electric field. This significant difference leads to a different nonlinear model with its corresponding nonlinear equations that were briefly introduced in [26] and here are further discussed. Although the in-line model used in BAW resonators [19] and the crossed-field model for SAW devices are based on the same set of constitutive equations, using as independent variables the electric field E and the strain S, the nonlinear source T_{NL} (see Fig. 2) of the crossed-field model, does not depend on the nonlinear electrical displacement ΔD defined in [19], and the nonlinear source placed in the electric part of the Mason model of Fig. 2 is a nonlinear current source I_{NL} instead of a voltage source (see dashed box of Fig. 2). The reason is that the in-line model of BAW devices uses D and S as independent variables and therefore it does not have a straightforward implementation from the constitutive equation as the cross-field model has. Note that since the distributed circuit model is based on the Mason model, the following equations are implemented considering that the voltage represent the force and the current the particle velocity respectively.

The constitutive equations become nonlinear if additional terms ΔT and ΔD are introduced according to [20]:

$$T = c^E S - eE + \Delta T \qquad (3)$$

$$D = eS + \varepsilon^S E + \Delta D, \qquad (4)$$

where, following the nomenclature of [21], these nonlinear terms ΔT and ΔD, truncated to a third-order polynomial, are

$$\Delta T = c_{2,MR}^E \frac{S^2}{2} + c_{3,MR}^E \frac{S^3}{6} - \phi_{3,MR} \frac{E^2}{2} + \phi_{5,MR} SE$$
$$- X_{9,MR} \frac{S^2 E}{2} + X_{7,MR} \frac{E^2 S}{2} - e_{3,MR}^E \frac{E^3}{6} \qquad (5)$$

$$\Delta D = \varepsilon_{2,MR}^S \frac{E^2}{2} + \varepsilon_{3,MR}^S \frac{E^3}{6} - \phi_{5,MR} \frac{S^2}{2} + \phi_{3,MR} SE + X_{9,MR} \frac{S^3}{6} -$$
$$X_{7,MR} \frac{S^2 E}{2} + e_{3,MR}^E \frac{SE^2}{2},$$

being those nonlinear terms defined by several second-order ($c_{2,MR}^E$, $\phi_{3,MR}$, $\phi_{5,MR}$, $\varepsilon_{2,MR}^S$) and third-order ($c_{3,MR}^E$, $\varepsilon_{3,MR}^S$, $X_{9,MR}$, $X_{7,MR}$, $e_{3,MR}^E$) coefficients.

Scaling (3) by $-A_L$ we obtain

$$-A_L T = -A_L c^E S + A_L eE - \Delta T A_L, \qquad (6)$$

and this equation is fulfilled in the Mason model of Fig. 2, where a nonlinear voltage source $T_{NL} = \Delta T \cdot A_L$ has been included. Note that (6) considers propagation without losses for simplicity. Losses, which are included in Fig. 2, can be easily included considering a complex elastic constant in (6) as described in [31]. With regards to the electric part of the Mason

model, scaling (4) by the area of the electrode and taking its time derivative in phasor form we can write:

$$-j\omega DA = -j\omega eSA - j\omega\varepsilon^{S}EA - j\omega\Delta DA, \qquad (7)$$

where the left-hand side of the above equation represents the total current I trough an area $A = w\Delta z$ as depicted in Fig. 1(a). Equation (7) indicates that an additional current source $I_{NL} = -j\omega \cdot A \cdot \Delta D$ in parallel with the electrostatics capacitance must be included in the Mason model as depicted in Fig. 2.
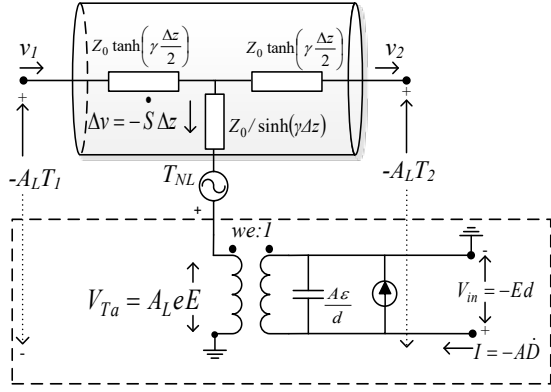

Fig. 2. Nonlinear unit cell of the MR section of an electrode [26].

The equations and model of the NMR sections, whose unit-cell is depicted in Fig. 3, are much simpler because only acoustic wave propagation is considered. The nonlinear Hooke's law up to a third order expansion is:

$$T = cS + T_{NL} \qquad (8)$$

$$T_{NL} = \frac{1}{2}c_{2,NMR}S^{2} + \frac{1}{6}c_{3,NMR}S^{3},$$

where $c, c_{2,NMR}$ and $c_{3,NMR}$ correspond to the elastic constants of a given material and its nonlinear derivatives.
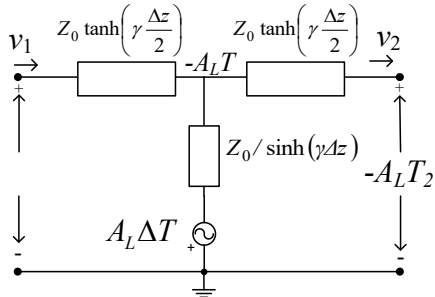

Fig. 3. Nonlinear unit cell of the NMR section.

1) Modelling of a λ-section

The active resonator's area can be represented using an equivalent circuit for an IDT composed of M λ-sections. Figure 4 (b) shows a λ-section formed by two MR sections (two digits) and tree NMR sections for the acoustic propagation. Note that the far right and left side boxes are denoted as NMR/2 just to illustrate that the length of those sections is half the separation between fingers since we are cascading identical λ-sections to form the IDT. MR and NMR sections are connected in cascade for the acoustic propagation and the two digits of a period are connected changing the polarity as depicted in Fig. 4 (b). Note that Fig. 4 depicts the specific case of a one-port resonator with one of the electrical ports connected to ground.

Figure 4 (c) shows how the MR and NMR are discretized into many unit cells (N) to account for the distributed nonlinear
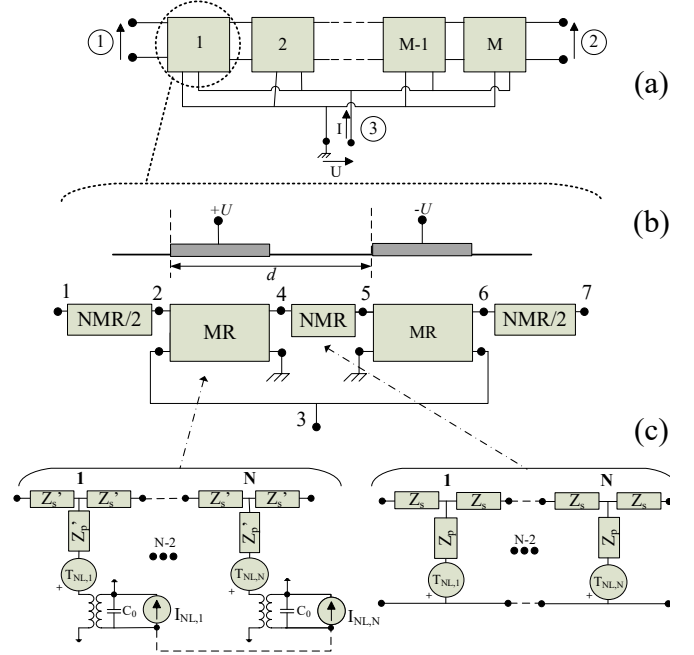
sources, which depend on the local field magnitudes.

Fig. 4. (a) Schematic of the reference SAW resonator for M λ-sections connected acoustically in cascade and electrically in parallel. (b) Example of the equivalent circuit for a λ-section (period) with two electrodes. (c) Both MR and NMR are composed of N nonlinear unit-cells.

2) Modelling of M λ-sections

The whole transducer is made up of M λ-sections as Fig. 4 (a) depicts. Therefore, if a resonator is comprised by, for example, one hundred λ-sections and let us assume that each λ-section requires at least 40 unit-cells (as it will be discussed in subsection III.E.2), the simulation of the distributed model (4.000 nonlinear unit-cells) using commercial software becomes unfeasible. In this context, it is worth to analyze the circuit using the IOES method.

III. IOES METHOD APPLIED TO A SAW RESONATOR

The analysis of large distributed problems has been previously reported in [25] and [26] by taking advantage of the weak nonlinear behavior of these passive devices. According to the perturbation theory, the circuit can be linearly solved at the fundamental frequencies and then the perturbation solution can be obtained taking into consideration the nonlinear terms of the constitutive equations.

In distributed problems, the field magnitudes are found at any point of the discretized circuit and the nonlinear sources of a given H/IMD are calculated in the frequency domain to finally analyze the circuit at those frequencies and obtain the output power at the load. Moreover, the generation of the H's or IMD's might be caused by direct generation involving only the fundamental frequencies or by the so-called remix effects meaning that, for example, a generated second order intermodulation product (IMD2) can be remixed with a fundamental signal to create an IMD3.

The procedure of the IOES method can be outlined as

follows:

1. The whole resonator is linearly evaluated at the fundamental frequencies without discretizing the regions. The magnitudes of interest -independent variables of the nonlinear equations- are then found at the boundaries of each region.
2. Using these boundary magnitudes, the standing wave patterns -field magnitudes strain $S(z)$ and electric field $E(z)$ at each position along the propagating direction- are mathematically calculated following conventional circuit analysis [32].
3. The distributed nonlinear sources at each position are then calculated at a given H or IMD in the frequency domain (weak nonlinear approach).
4. The corresponding IOES sources applied at the boundaries of each region -producing the same effect as all the distributed nonlinear sources- are then calculated.
5. The non-discretized circuit is then analyzed at the targeted IMD/H frequencies using these IOES sources.

This section applies the IOES method of [25] to SAW resonators providing further details than those appearing in [26], where the IOES method was very briefly described. The new details are:

- We provide all the equations required to obtain the field magnitudes at any point as a function of the boundary magnitudes.
- We further detail the frequency-domain equations of the nonlinear sources, including remix effects.
- The reflectors are considered nonlinear.
- An analysis of the required minimum number of unit-cells is shown to get shape-independent nonlinear parameters.
- A characterization process of the IMD3 response to identify potential contributors is fully described.
- Linear and nonlinear analysis of two different sets of resonators with different pitch and duty factor are provided.

A. Step 1. Analyzing the non-discretized circuit

The non-discretized circuit is characterized by its admittance matrix denoted as $[\mathbf{Y}_\omega]$, where ω refers each frequency component of interest. This admittance matrix is created by joining the matrix of each different region, which are calculated independently as detailed in Appendix I. Then, the circuit is linearly analyzed at each fundamental frequency to obtain voltages and currents at the boundaries of each region.

It is important to outline that, as the circuit is not fully discretized, this step is faster in comparison with evaluating the full discretized circuit as it was done in [22] or typically done with a commercial simulator using HB techniques.

B. Step 2. Standing wave pattern calculation

The voltages obtained at the boundaries of each section of the equivalent circuit (each of the nodes of Fig. 4 (b)) are used to calculate the field distribution as a function of the position z inside a given nonlinear section. The number of discrete positions is called the discretization number N.

At this point, it is worth mentioning that the process to obtain the standing wave patterns at a targeted frequency for remix purposes is slightly different. The nonlinear generators at an intermediate frequency must be taken into consideration when calculating the standing wave pattern at this intermediate frequency. The intermediate frequencies are those that are remixed with the fundamental tones to generate a targeted IMD3. This process is completely described in Appendix II.

1) Non-metallized region

The voltage (force) distribution along the NMR sections, as it corresponds to a conventional transmission line (TL), will be:

$$V(z) = \frac{V_1 e^{\gamma z_2} - V_2 e^{\gamma z_1}}{2 sinh(\gamma(z_2 - z_1))} e^{-\gamma z} + \frac{V_1 e^{-\gamma z_2} - V_2 e^{-\gamma z_1}}{2 sinh(\gamma(z_1 - z_2))} e^{\gamma z} \quad (9)$$

being V_1 and V_2 the voltages at both ends (positions z_1 and z_2 and $\Delta z = z_2 - z_1$) of the TL, that is, input and output nodes of the NMR section, and γ is the propagation constant associated to the NMR region. After that, the strain at each point of the NMR section $S(z)$ can be found considering the voltage at the junction of the T-network of Fig. 3, which is denoted as $V_c(z)$, and c^E, following:

$$S(z) = -\frac{V_c(z)}{A_L c^E}$$
$$= -\frac{\left(V\left(z - \frac{\Delta z}{2} \right) + V\left(z + \frac{\Delta z}{2} \right) \right)}{2 cosh^2 \left(\gamma \frac{\Delta z}{2} \right) A_L c^E} \quad (10)$$

where, A_L is the lateral resonator area (see Fig. 1 left), and c^E is the elastic constant.

2) Metallized region

For the MR section we will consider four boundary nodes, the ones corresponding to the acoustic part (V_1 and V_2) and the ones of the electrical part (V_3 and V_4). First, the voltage at the acoustic part of the transformer (Fig. 2) is calculated by using

$$V_{Ta} = \pm T V_{in} \quad (11)$$

where T is the transformer ratio of the Mason model of Fig. 2, V_{in} corresponds to the electrical input port of the electrodes (port 3 in Fig. 4 (b)), and the sign $\pm$ depends on the polarization of the electrodes in a λ-section. Therefore, knowing (11) and introducing it into (9) we get $V(z)$:

$$V(z) - V_{Ta}$$
$$= \frac{(V_1 - V_{Ta})e^{\gamma z_2} - (V_2 - V_{Ta})e^{\gamma z_1}}{2 sinh(\gamma(z_2 - z_1))} e^{-\gamma z}$$
$$+ \frac{(V_1 - V_{Ta})e^{-\gamma z_2} - (V_2 - V_{Ta})e^{-\gamma z_1}}{2 sinh(\gamma(z_1 - z_2))} e^{\gamma z} \quad (12)$$

and the strain $S(z)$ is calculated as it was done before using (10).

The electric field is found directly from the input voltage since the opposite electrical port to the input port is grounded (see Fig. 4 (c)).

$$E(z) = \pm \frac{1}{d} V_{in} \quad (13)$$

Where d is the spacing between electrode centers (pitch). Note that we assume that the electric field distribution is constant

below the metallized regions. This is of course a rough approximation to a real interdigital transducer, but as it will be shown in later sections, this approach is good enough to model the IMD3 of SAW resonators. The circuit model could be extended to account for non-uniform electric fields, but this is beyond the scope of this article where we try to keep the circuit model as simple as possible.

C. Step 3. Distributed nonlinear sources

An alternative method based on Volterra series analysis is used to simulate weak nonlinear circuits [33]. Frequency-domain equations in the steady state are mathematical expressions that provide closed-form expressions of a given H or IMD for weak nonlinearities.

1) Direct generation

In the SAW case, third-order nonlinear signals like IMD3 or third order harmonics (H3) are the main concern in terms of nonlinear distortion as H2 (or IMD2) generation have less impact due to its own cancellation nature [34], [35]. In this article we restrict the analysis to the IMD3.

The nonlinear equations related to the directly generated IMD's products in the MR due to the third order terms of (5) are

$$\Delta T_{2\omega_2 - \omega_1} = \frac{1}{8} c^E_{3,MR} S^2_{\omega_2} S^*_{\omega_1} - \frac{3}{8} X_{9,MR} S^2_{\omega_2} E^*_{\omega_1} + \frac{3}{8} X_{7,MR} E^2_{\omega_2} S^*_{\omega_1}$$
$$- \frac{1}{8} e^E_{3,MR} E^2_{\omega_2} E^*_{\omega_1}$$
$$\Delta D_{2\omega_2 - \omega_1} = \frac{1}{8} \varepsilon^S_{3,MR} E^2_{\omega_2} E^*_{\omega_1} + \frac{1}{8} X_{9,MR} S^2_{\omega_2} S^*_{\omega_1} - \frac{3}{8} X_{7,MR} S^2_{\omega_2} E^*_{\omega_1}$$
$$+ \frac{3}{8} e^E_{3,MR} E^2_{\omega_2} S^*_{\omega_1} \tag{14}$$

where ω_1 and ω_2 correspond to the fundamental frequencies in a standard two-tone experiment, being $\omega_2 > \omega_1$. Similar expressions could be written for the terms $2\omega_1 - \omega_2$ (swapping the subscripts) and $2\omega_1 + \omega_2$, $2\omega_2 + \omega_1$. In these two later cases none of the phasors S and E are conjugated [33].

For the case of the NMR sections the equation is much simpler and becomes:

$$\Delta T_{2\omega_2 - \omega_1} = \frac{1}{8} c_{3,NMR} S^2_{\omega_2} S^*_{\omega_1} \tag{15}$$

2) Remix generation

All the second order H's and IMD's that could remix to cause third order IMD3 must be calculated. Those terms correspond to the frequencies $2\omega_1$, $2\omega_2$, $\omega_2 - \omega_1$, $\omega_1 + \omega_2$.

For the H2 case we will use the following equations for the MR section:

$$\Delta T_{2\omega_1} = \frac{1}{4} c^E_{2,MR} S^2_{\omega_1} + \frac{1}{4} \phi_{3,MR} E^2_{\omega_1} + \frac{1}{2} \phi_{5,MR} S_{\omega_1} E_{\omega_1} \tag{16}$$

$$\Delta D_{2\omega_1} = \frac{1}{4} \varepsilon^S_{2,MR} E^2_{\omega_1} - \frac{1}{4} \phi_{5,MR} S^2_{\omega_1} + \frac{1}{2} \phi_{3,MR} S_{\omega_1} E_{\omega_1} \tag{17}$$

and for the NMR section:

$$\Delta T_{2\omega_1} = \frac{1}{4} c_{2,NMR} S^2_{\omega_1} \tag{18}$$

For the case of the IMD2 $\omega_2 - \omega_1$ we will use the following equations for the MR section:

$$\Delta T_{\omega_2 - \omega_1} = \frac{1}{2} \phi_{5,MR} (S_{\omega_2} E^*_{\omega_1} + E_{\omega_2} S^*_{\omega_1}) + \frac{1}{2} c^E_{2,MR} (S_{\omega_2} S^*_{\omega_1}) \tag{19}$$
$$+ \frac{1}{2} \phi_{3,MR} (E_{\omega_2} E^*_{\omega_1})$$

$$\Delta D_{\omega_2 - \omega_1} = -\frac{1}{2} \phi_{5,MR} (S_{\omega_2} S^*_{\omega_1}) + \frac{1}{2} \varepsilon^S_{2,MR} (E_{\omega_2} E^*_{\omega_1}) \tag{20}$$
$$+ \frac{1}{2} \phi_{3,MR} (E_{\omega_2} S^*_{\omega_1} + E^*_{\omega_1} S_{\omega_2})$$

and for the NMR section:

$$\Delta T_{\omega_2 - \omega_1} = \frac{1}{2} c_{2,NMR} S_{\omega_2} S^*_{\omega_1} \tag{21}$$

The terms of $\omega_1 + \omega_2$ are straightforward obtained avoiding conjugating any phasor.

Once the whole circuit is evaluated for those second order H's and IMD's, the sources of IMD3 due to remix effects can be calculated considering all the combinations of frequencies that might contribute to a given IMD3. For example, the sources of IMD3 at $2\omega_2 - \omega_1$ will be:

$$\Delta T_{2\omega_2 - \omega_1} = \frac{1}{2} \phi_{5,MR} (S_{2\omega_1} E^*_{\omega_2} + S^*_{\omega_2} E_{2\omega_1} + S_{\omega_1} E^*_{\omega_1 - \omega_2} + S^*_{\omega_1 - \omega_2} E_{\omega_1})$$
$$+ \frac{1}{2} C^E_{2,MR} (S_{2\omega_1} S^*_{\omega_2} + S_{\omega_1} S^*_{\omega_1 - \omega_2}) \tag{22}$$
$$- \frac{1}{2} \phi_{3,MR} (S_{2\omega_1} S^*_{\omega_2} + S_{\omega_1} S^*_{\omega_1 - \omega_2})$$

$$\Delta D_{2\omega_2 - \omega_1} = -\frac{1}{2} \phi_{5,MR} (S_{2\omega_1} S^*_{\omega_2} + S_{\omega_1} S^*_{\omega_1 - \omega_2})$$
$$+ \frac{1}{2} \varepsilon^S_{2,MR} (E_{2\omega_1} E^*_{\omega_2} + E_{\omega_1} E^*_{\omega_1 - \omega_2}) \tag{23}$$
$$+ \frac{1}{2} \phi_{3,MR} (S_{2\omega_1} E^*_{\omega_2} + S^*_{\omega_2} E_{2\omega_1} + S_{\omega_1} E^*_{\omega_1 - \omega_2}$$
$$+ S^*_{\omega_1 - \omega_2} E_{\omega_1})$$

and for the NMR sections:

$$\Delta T_{2\omega_1 - \omega_2} = \frac{1}{2} c_{2,NMR} (S_{2\omega_1} S^*_{\omega_2} + S_{\omega_1} S^*_{\omega_1 - \omega_2}) \tag{24}$$

D. Step 4. Input-Output Equivalent Sources

The input-output equivalent nonlinear currents sources are found applying a rigorous mathematical procedure. As mentioned before, these equivalent nonlinear sources cannot lose the distributed nature of the problem. The powerful of the IOES method consists of calculating the equivalent sources at given boundaries that account for all the distributed nonlinear sources between these boundaries. This can be done without inverting big matrices and the procedure is based on an ABCD matrix description of the NMR sections and a 4-port ABCD matrix description of the MR sections.

1) IOES of a non-metallized region

The linear circuit is analyzed at the fundamental frequencies of a source connected to the port V_{in} (node 3 in Fig. 4 (b)) getting all the voltages and currents associated to each boundary node.

As an example, let us assume that we want to calculate the nonlinear contribution of the central NMR just between the electrodes, that is between nodes 4 and 5 of Fig. 4 (b). By means of (9) and (10), it is possible to calculate the strain $S_{\omega_1}(z)$ and $S_{\omega_2}(z)$, and then, to find the distributed nonlinear sources $T_{NL}(z)$ at a given IMD following (15).

Now, the conventional ABCD relation between the voltage-current vector at the input and at the output of a transmission line (NMR unit-cell) of length Δz at the position z_i must be modified to include the corresponding nonlinear source at that position:

$$\begin{bmatrix} V_{1,i} \\ I_{1,i} \end{bmatrix} = [ABCD]_{\Delta z} \begin{bmatrix} V_{2,i} \\ I_{2,i} \end{bmatrix} + \begin{bmatrix} -\frac{z_{s,i}}{z_{p,i}} \\ 1 \\ -\frac{1}{z_{p,i}} \end{bmatrix}_{\Delta z} T_{NL}(z_i) \tag{25}$$

where $[ABCD]_{\Delta z}$ is the conventional ABCD matrix of a TL of length Δz, and $z_{s,i}$ and $z_{p,i}$ are the series and shunt acoustic impedance of the T-network (see Appendix III. A). Note that $z_{s,i}$ and $z_{p,i}$ are always the same (for any i value) and

corresponds to one unit-cell, therefore from now on, they will be denoted as z_s and z_p for simplification.

This description of a unit-cell allows to cascade N identical cells. The mathematical procedure is not straightforward due to the addition of the nonlinear source. However, it can be done as detailed in Appendix III. A resulting in a very simple expression that relates the V-I vector of the input port with the V-I vector of the output port as:

$$\begin{bmatrix} V_1 \\ I_1 \end{bmatrix} = [ABCD]_{\Delta z}^N \begin{bmatrix} V_{N+1} \\ I_{N+1} \end{bmatrix} + \begin{bmatrix} V_{eq} \\ I_{eq} \end{bmatrix} \quad (26)$$

The terms V_{eq}, I_{eq} accounts for the contribution of all the distributed nonlinear sources. Note that the matrix $[ABCD]_{\Delta z}^N = [ABCD]_{N\Delta z}$ is the one that corresponds to the conventional ABCD matrix of the whole section (a TL of length $N \cdot \Delta z$), which can be easily calculated without multiplying the matrices of the N unit-cells.

Certainly, (26) could be used to evaluate an equivalent circuit that concentrates all the nonlinearities in two equivalent sources as in Fig. 5(a). Nevertheless, and due to the use of the Y matrix description of the whole circuit, it is more convenient to turn these two sources V_{eq}, I_{eq} into two current sources I_{e1}, I_{e2} as depicted in Fig. 5 (b).
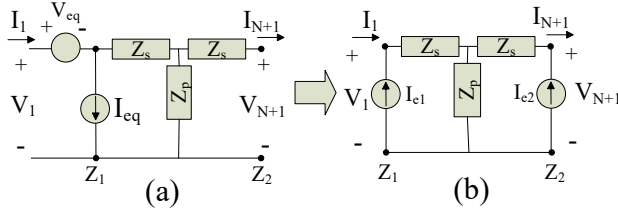

Fig. 5. Current equivalent sources of a non-metallized region.

This can be done (as shown in Appendix III.A) by means of

$$I_{e1} = \frac{1}{z_s + 2z_p}\left(1 + \frac{z_p}{z_s}\right)V_{eq} - I_{eq}$$
$$I_{e2} = \frac{-1}{z_s + 2z_p}\left(\frac{z_p}{z_s}\right)V_{eq} \quad (27)$$

where z_s and z_p correspond to the whole section of length $N \cdot \Delta z$.

2) IOES of a metallized region

Analogously to the NMR sections, the voltages and currents that are found at the four nodes of the MR section (see Fig. 4 (b)) will allow to calculate the independent variables $S(z)$ and $E(z)$ (section III.B.2) to further find the nonlinear sources $T_{NL}(z)$ and $I_{NL}(z)$ at a given H/IMD (section III.C).

The IOES of the MR sections and its associated pseudo ABCD matrix equations has been previously reported in [26]. The procedure is the same than the one described for the NMR sections and all the steps involved are detailed in Appendix III.B for completeness of this article. The counterpart equations to (25), (26) are:

$$\begin{bmatrix} V_{1,i} \\ I_{1,i} \\ V_{3,i} \\ I_{3,i} \end{bmatrix} = [4ABCD]_{\Delta z}\begin{bmatrix} V_{2,i} \\ I_{2,i} \\ V_{4,i} \\ I_{4,i} \end{bmatrix} + \begin{bmatrix} -\frac{z_{s',i}}{z_{p',i}} \\ 1 \\ -\frac{1}{z_{p',i}} \\ 0 \\ T \\ -\frac{T}{z_{p',i}} \end{bmatrix} T_{NL}(z_i) + \begin{bmatrix} 0 \\ 0 \\ 0 \\ 1 \end{bmatrix} I_{NL}(z_i) \quad (28)$$

$$\begin{bmatrix} V_{1,1} \\ I_{1,1} \\ V_{3,1} \\ I_{3,1} \end{bmatrix} = [4ABCD]_{\Delta z}^N\begin{bmatrix} V_{2,N+1} \\ I_{2,N+1} \\ V_{4,N+1} \\ I_{4,N+1} \end{bmatrix} + \begin{bmatrix} V_{1,eq} \\ I_{1,eq} \\ 0 \\ I_{3,eq} \end{bmatrix} \quad (29)$$

Detailed expressions of the calculus of (29) can be found in Appendix III.B and the equivalent current sources are as shown in Fig. 6 left.

As it was done for the NMR, we are interested in an all-current source's solution (Fig. 6 right). The corresponding equations explaining the relation between the equivalent current sources are as follows

$$I_{eq1} = \left(\frac{z_{p'}}{z_{s'}} + 1\right)\frac{V_{1,eq}}{\left(\frac{z_{s'}^2}{z_{p'}} + 2z_{s'}\right)} - I_{1,eq}$$

$$I_{eq2} = -\frac{V_{1,eq}}{\left(\frac{z_{s'}^2}{z_{p'}} + 2z_{s'}\right)} \quad (30)$$

$$I_{eq3} = \left(\frac{Tz_{p'}}{z_{s'}}\right)\frac{V_{1,eq}}{\left(\frac{z_{s'}^2}{z_{p'}} + 2z_{s'}\right)} - I_{3,eq}$$
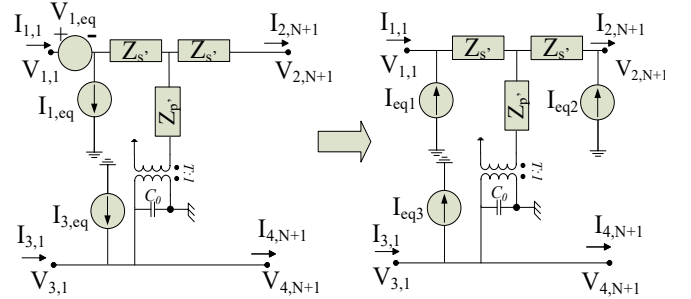

Fig. 6. IOES of a MR section.

Finally, Fig. 7 shows the IOES of a λ-section (only sources of one MR and one NMR are shown for clearness of the figure). The currents that apply to the same boundary nodes are added to form a vector of source currents $[I_\omega]_{7x1}$ at any of the frequencies ω to be calculated. This vector of currents is then used to get the node voltages at each node by means of the admittance matrix $[\mathbf{Y}_\omega]_{7x7}$. Details of how this admittance matrix is built up can be found in Appendix I.

$$[V_\omega]_{7x1} = [\mathbf{Y}_\omega]_{7x7}^{-1} \cdot [I_\omega]_{7x1} \quad (31)$$
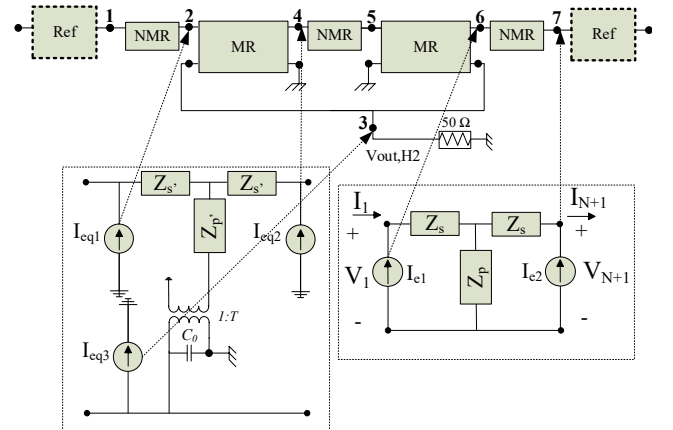

Fig. 7. IOES of both MR and NMR sections applied to a λ-section..

3) IOES method for M λ-sections

Once the analysis of a λ-section has been derived, we can cascade the M λ-sections to analyze the whole resonator. The result is a new admittance matrix $[\mathbf{Y}_\omega]_{(5\cdot M+2))x(5\cdot M+2))}$ that is built up from the admittances matrices of the λ-sections just considering that the last and first acoustic nodes of each consecutive section must be connected and all the electric nodes of each section must be connected to the same input node corresponding to the node 3 of Fig. 4.

When the whole non-discretized circuit is evaluated for the fundamental frequencies, the IOES equivalent sources of each section can be calculated as described in the previous sections. Note again, that the nonlinear current sources of two λ-sections that are connected to a given node must be added to get finally the $5M + 2$ vector of currents at a given targeted IMD3 or H.

4) IOES method for SAW resonators: IDT and reflectors

Following the same process described for the IDT, we can cascade R times λ/2-sections of the reflector with 4 additional nodes per section. The result is a new admittance matrix $[\mathbf{Y}_{\mathbf{r},\omega}]_{PxP}$ of dimension $P = 2(3 \cdot R + 1) + (5 \cdot M + 2) - (2)$, the first addend considers the reflectors on each side of the IDT, the second addend the IDT section and the last addend accounts for the common nodes between IDT and reflectors.

At this point we outline that the maximum dimension of the matrix to be inverted is P, instead of $N\cdot P$ as it would correspond to the whole solution without using the IOES method, which results in a drastic reduction of the computing time.

E. Step 5. IOES method validation

The IOES method has been validated trough comparisons with ADS [36] obtaining the same results. In all the cases a two-tone experiment with 51 frequency points is performed and, for a fair comparison between both methods, all the possible H's and IMD products were considered including remix effects as it was done in [25].

1) Computing time comparison with ADS

We have compared several examples using a general-purpose computer with an Intel Core i7-10750H CPU @ 2.60 GHz and 32 GB RAM. Moreover, we have progressively increased the number of λ-sections: M=1, 5 and 100. The discretization level was set to N=100 unit-cells per MR section and NMR section, which means 400 unit-cells per λ-section following the picture shown in Fig. 4. For the simulations of M=1 and 5 it has been previously checked that both ADS and IOES traces perfectly overlap. ADS simulations of 1 and 5 λ-sections take 130.3 s and 3330.1 s respectively, whereas the IOES using Matlab® R2018b [37] takes 1.6 s and 3.3 s respectively. Note that the IOES simulations are performed without using parallel computing. That is, the IOES method is around 80 and 1000 times faster than HB being this difference more noticeable as the number of electrodes increases since the IOES method does not increase O(N^2) with the problem size. For the case of 100 λ-sections, simulations using ADS were unaffordable, whereas IOES takes 133.2 s.

2) Discussion about the minimum number of unit-cells

Although the discretization level N does not affect to the size of the matrix to be inverted when analyzing the circuit using the IOES method, it obviously has an impact on the computing time

required to calculate the equivalent sources. In this subsection we discuss about the minimum number of unit-cells per region to achieve accurate results for the IMD3 and minimizing the computing time.

Fig. 8 shows simulations of a resonator with a duty factor of 50%. In this example we have used a third order coefficient of the elastic constant for the MR $c_{3,MR}^E$, and NMR $c_{3,NMR}$ published in [26]. Red, blue, green and black dashed trace represents IOES simulations of the IMD3 with a discretization of 1, 2, 10 and 20 unit-cells per region respectively. As it can be seen, changes in the number of cells for the discretization leads to significant differences in the response below N=10 (green dashed trace). Note that for the case of N=20 (red dashed trace) the results are almost identical with N=10, therefore 10 unit-cells is considered a good number that provides a good compromise between computing time of the IMD3 and accuracy. Note that the required degree of discretization could be higher if the targeted frequency was higher, as it would be the case of the third harmonic for example.
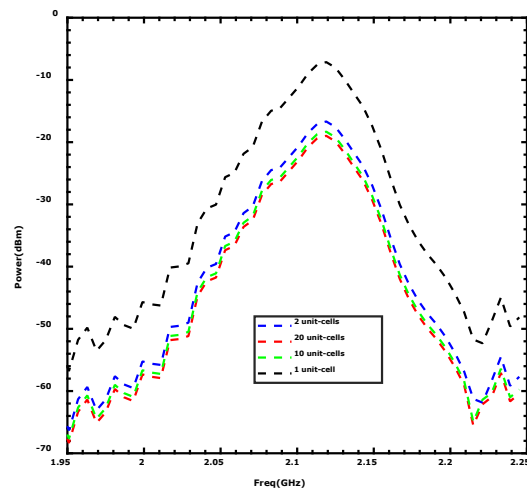

Fig. 8. Simulated variation of 3rd order IMD response of a η=50% SAW resonator. Black, blue, green and red dashed traces correspond to a simulated ($2f_2$-f_1) response with 1, 2 ,10 and 20 unit-cells, respectively.

Fig. 8 reveals that the shape of the frequency pattern of the IMD3 response within this narrow frequency range is quite independent of the discretization level. However, the IMD3 level is overestimated unless the discretization level was high enough. This figure unveils the importance of the distributed models because the material parameter that causes a given nonlinear phenomenon must be independent of the discretization level. In fact, a given nonlinear parameter of the local constitutive equations must be consistent with the nonlinear phenomena appearing in different resonators with other geometries. This is essential in order to predict the nonlinearities in new devices before manufacturing them.

Table I shows an analysis of the robustness of the distributed model. As a reference, let us consider a SAW resonator with a pitch of 950 nm and a duty factor of 50% simulated with N=10. Then, we have performed simulations of several resonators changing the pitch and the duty factor and we have obtained the $c_{3,MR}^E$ parameter that provides the same IMD3 level than the one of the reference resonator. Table I shows the absolute percent variation of this parameter respect the value of the reference resonator changing the number of N. As it can be seen the error

considering only 1 cell can be even higher than 800% and almost 40% for $N=2$ simulations.

The relative error is calculated with respect to the required value with the same number of cells of the reference resonator and it quantifies the capability of the model to deal with different geometries. If we consider only 1 unit-cell per region, the term $c_{3,MR}^{E}$ may change up to an 88% for different geometries. The shape independent capability of the model is reduced up to a 6% percent if just 2 unit-cells are considered.

This analysis allows to set the value of $N=10$ per region (which corresponds with 40 unit-cell per λ) as a conservative value that guarantees independency of the model with the discretization level and the shape of the resonator.

TABLE I
VARIATION OF NL COEFFICIENT $c_{3,MR}^{E}$ WITH THE NUMBER OF CELLS WITH RESPECT OF A 10 CELL CASE

Resonator		Absolute error [%]		Relative Error [%]	
Pitch [nm]	$\eta(\%)$	2 cells	1 cell	2 cells	1 cell
950	40	30.3	155.59	1.14	34.31
	45	25.0	198.80	5.16	23.21
	50	31.8	289.11	-	-
	55	35.7	433.33	2.93	37.07
	60	39.7	632.82	5.96	88.34
	65	21.3	896.68	7.95	156.15
850	50	30.2	332.81	1.26	11.23
900	50	30.2	319.57	1.26	7.83
1000	50	30.8	318.12	0.80	7.46
1100	50	30.8	313.81	0.80	6.35

Note that a full simulation of a SAW resonator composed by an IDT region of $M=100$ pair of electrodes and each reflector region with 20 electrode pairs and a discretization of $N=10$ unit-cells per section results in a 5600 cells nonlinear problem. This results in an unfeasible large problem to be evaluated using conventional Harmonic Balance techniques, whereas the IOES method spend 35.4 s (51 frequency points) to evaluate all the possible nonlinear harmonics and intermodulation products up to a third order.

IV. EVALUATION OF SIMULATION AND MEASUREMENT RESULTS

This section starts with a description of the evaluated set of resonators and their measured and simulated linear responses. Once the linear model is validated, an extensive characterization process of the in-band IMD3 response is described to figure out which is the nonlinear parameter that better agrees with the measured in-band IMD3 of a reference resonator. Finally, this characterization process is validated with simulations and measurements of other resonators with different geometry.

A. Description of resonators

Several one-port LSAW resonators for the LTE B66 band were measured. Those resonators cover a frequency range from 1.7 to 2.6 GHz and use the same LiTaO$_3$ 42-cut substrate. All the devices are composed by 100 electrode pairs ($M=100$) in the IDT region and 20 electrode pairs ($R=20$) in each reflector. The aperture is $20 \cdot \lambda$ with a variable pitch from 850 to 1100 nm and different duty factors. The metallization of the electrodes is made by an aluminum-based metal stack.

The tested devices, which were arbitrarily chosen from different parts of the wafer, are classified into 2 sets. The first set corresponds to six resonators with the same pitch of 950 nm and different duty factor: 40%, 45%, 50%, 55%, 60% and 65%. The second set is composed by four resonators with different pitch from 850 to 1100 nm and a duty factor of 50 %.

B. Linear response

Prior to proceed with the nonlinear characterization of the devices, the linear model, described in Section II.A, must be able to reproduce the linear response of the resonators. Fig. 9, and Fig. 10 depicts the agreement of the measured input admittance (blue trace) and simulations (red trace) of the resonators corresponding to Set 1 and Set 2, respectively. Note that in both Fig. 9 and Fig. 10 an artificial offset (a factor 1/10 per resonator and -10 degrees per resonator respectively) was added for easy viewing of the traces.
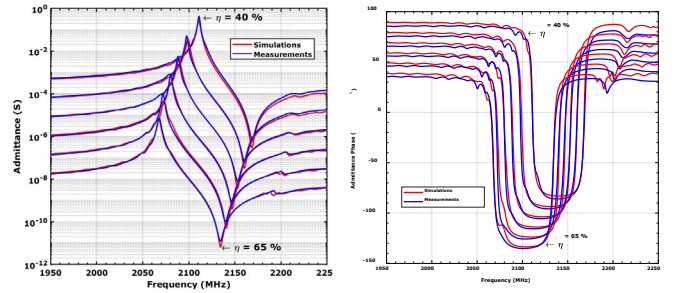

Fig. 9. Measured (blue trace) and simulated (red) input admittance magnitude on the left and admittance phase on the right of the measured resonators of Set 1 having same pitch and different duty factor.
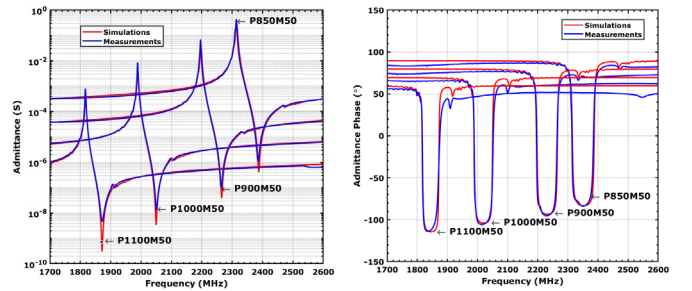

Fig. 10. Measured (blue trace) and simulated (red) input admittance magnitude on the left and admittance phase on the right of the measured resonators of Set 2 having a fixed duty factor of 50 % and a variable pitch.

Table II shows the linear parameters corresponding to the phase velocities for each region V_{MR} and V_{NMR}, the equivalent for the reflectors V_{MRr} and V_{NMRr}, the effective relative dielectric constant ϵ_r and the piezoelectric constant e. The last four rows correspond to the Set 2 resonators where P refers to the pitch and M to the duty factor. With regards to Set 1, all the six resonators are simulated with the same parameters but the effective dielectric constant ϵ_r. The total capacitance of the IDT is very roughly calculated using the simple expression $C_0 = \epsilon_{r,eff} \cdot \epsilon_0 \frac{A}{d \cdot M}$, where A and d correspond to the in-plane area and pitch (Fig. 1 (a) and Fig. 4 (b)) respectively. As discussed in section II.A, the relative dielectric constant must be

considered as an effective parameter that is fine tuned for each resonator. Despite of this simple approach of the total IDT capacitance, this parameter is within the range between 47 and 50 for all the resonators with different duty factor (Set 1) while it scales very well with the pitch since $\epsilon_{r,eff} = 48$ is used for all the Set 2 resonators.

TABLE II
SAW RESONATORS LINEAR PARAMETERS

Resonator	V_{MR} [m/s]	V_{NMR} [m/s]	$V_{MRr}/$ V_{MR} [m/s]	$V_{NMRr}/$ V_{NMR} [m/s]	$\epsilon_{r,eff}$	e
Set 1	3904	4318	1.035	0.954	47-50	1.95
P850M50	3875	4318	1.035	0.954	48	1.95
P900M50	3888	4318	1.035	0.954	48	1.95
P1000M50	3916	4318	1.035	0.954	48	1.95
P1100M50	3939	4318	1.035	0.954	48	1.95

Note that all the parameters of Set 2 are the same than those of Set 1 but small differences (within ±0.9%) in the velocities of the MR sections. We consider than these small variations are reasonable due to the simplicity of the model that assumes uniform electric field beneath the electrodes.

The values of the velocities into the reflector regions are tuned to reproduce the small spurious resonances appearing in the right side of the input admittance, close to the anti-resonance frequency. Note that these velocities have almost the same ratio respect to their counterparts of the active area. This slight difference could be explained by small influences of the electric field into the wave velocities in the MR and NMR.

Any parameter of a given resonator could be additionally fine-tuned to better reproduce the measurements. However, we decided to preserve the same parameters, but the ones mentioned above, to keep the simplicity of the model and demonstrate that despite of being a very simplified equivalent circuit, the model is consistent enough to reproduce the narrowband response of the resonators.

Note that bulk-wave radiation [38] is not considered into this model. As stated in [38], this effect has a significant impact on the admittance of 42-LT SAW resonators, and it has less impact as the number of IDT finger pairs increases. Although the resonators we have measured have many electrode pairs (100), that is the reason that might explain the disagreement at frequencies above the antiresonance, between the measurements and the simulations. However, as it will be discussed into the following sections, it does not have a significant impact into the in-band IMD3.

C. IMD3 characterization process

A characterization process allows to discern which of the third-order nonlinear constants, or second-order constants that are involved in remix effects, plays a driving role in the IMD3 generation. This is done by comparing the frequency pattern of the measurements with the one produced by each nonlinear parameter and setting the other parameters to zero.

1) IMD3 measurements overview

The measurements consist of conventional two-tone experiments measuring the outgoing IMD3 power of a one-port resonator. The fundamental tones have 24 dBm of power (input

power to the device) and a constant tone spacing of $\Delta f = f_2 - f_1 = 10$ MHz. The central frequency was swept from 1.950 GHz to 2.250 GHz for the Set 1 measurements and from 1.680 GHz to 2.468 GHz for the Set 2. The IMD3 floor level of the measurement system was obtained with the probes on air, resulting in -80 dBm. Note that for a proper nonlinear fitting the effects of the measurement system are also included in the simulation. This is done by converting the measured 4-port S-parameters of the system to its corresponding Y-matrix [23], which is properly connected to the Y-matrix of the whole circuit model.

Fig. 11 shows the measured IMD3 for Set 1 (left) and Set 2 (right) resonators. All the measurements show a maximum IMD3 at a frequency between the series and shunt resonances, smaller peaks at higher frequencies that correspond to the frequencies of the small spurious resonances around 2.2 GHz after the shunt resonances already unveiled into the linear response, and a IMD3 plateau, between -50 dBm and -40 dBm at lower frequencies.
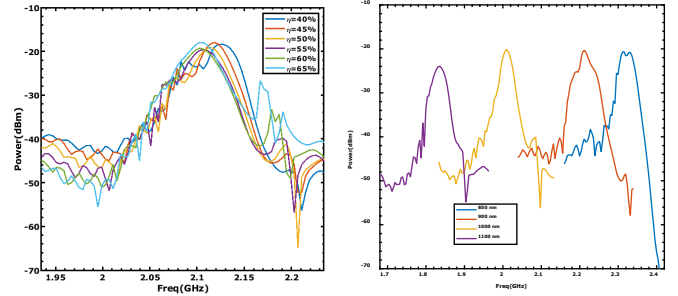

Fig. 11. IMD3 response of Set 1 (left) and Set 2 (right) measured resonators.

2) Identification of potential contributors

We decided to use as a reference resonator the one with pitch 950 nm and 50% of duty factor, whose measured IMD3 is shown in Fig. 12 with continuous green trace. Specifically, the frequency pattern of the second-order and third-order nonlinear derivatives of the stiffness, dielectric and piezoelectric constants are compared.

The upper plots of Fig. 12 show the simulated IMD3 response considering only the individual contribution of the third-order coefficients of (14), namely: $c_{3,MR}^E$ (red circle), $\varepsilon_{3,MR}^S$ (cyan dotted), $X_{7,MR}$ (magenta dotted) and $X_{9,MR}$ (black dot-dashed). The value of those coefficients was arbitrary set to provide a maximum IMD3 level comparable to the one measured to facilitate the comparison of their frequency mark with the measurements.

Note that the pattern of the values $\varepsilon_{3,MR}^S, X_{7,MR}$ and $X_{9,MR}$ exhibit a notch at the series resonance frequency and the one that provides the most similar frequency pattern is $c_{3,MR}^E$. Between the series and shunt resonances -marked with arrows into the figure- the value of $c_{3,MR}^E = -110c^E$ reproduces the same measured IMD3 very well.

Figure 12 also includes the trace for $c_{3,NMR} = -2100c$ of the NMR (blue dashed). As it can be seen, though the frequency pattern is very similar (except at higher frequencies where larger peaks appear) to the one caused by $c_{3,MR}^E$, it is necessary to force a very big value of $c_{3,NMR}$ to obtain the same maximum of IMD3. Certainly, these values could be slightly different in both regions since the mass loading of the electrodes could

affect to them. However, it seems there is no physical reason to force big differences between $c_{3,MR}^E$ and $c_{3,NMR}$. From now on, in all our simulations we will set the same value for both nonlinear constants.

It has been previously reported [23], [24] that the contribution of remix effects to the generation of IMD3 might be not negligible in comparison with the direct generation. At the bottom of Fig. 12 we have considered the second-order terms of the MR $\phi_{5,MR}$ (blue triangles) and $c_{2,MR}^E$ (orange diamonds), and the $c_{2,NMR}$ (yellow crosses) parameter of the NMR. Their values are arbitrary low for the clearness of the figure. It is clear than the frequency patterns that these parameters provide are not well correlated with the one measured, so we could conclude that, at least in this case, remix effects do not have an important effect on the IMD3 response and could be neglected.
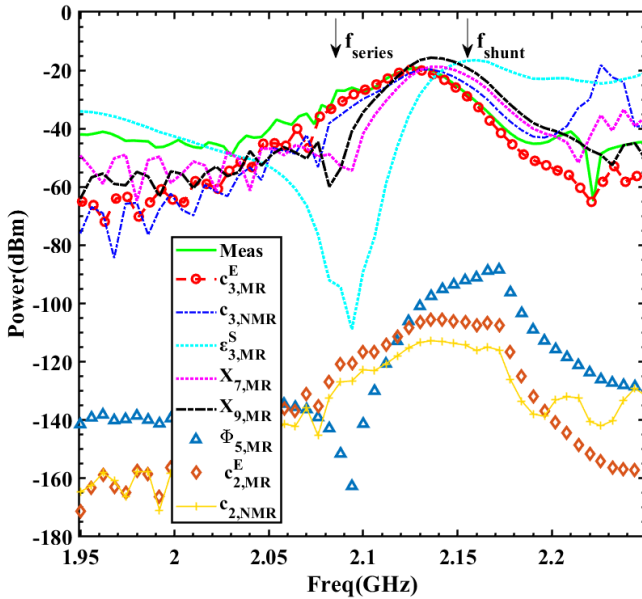

Fig. 12. Analysis example of a SAW reference resonator. Simulated IMD3 response of a SAW resonator. Green solid line corresponds to measured *2f1-f2* and red circle line to the best fitted data.

3) Reflector effects

Fig. 13 left shows with more detail the agreement between simulations and measurements of the in-band IMD3 response of the reference resonator using the values $c_{3,MR}^E = c_{3,NMR} = -110c^E$ we had got from the previous characterization process. Red and blue dashed traces correspond to computed *2f1-f2* and *2f2-f1* respectively, and measured response in green (*2f1-f2*) and magenta (*2f2-f1*) traces. Note that although simulations show pretty good in-band results there are still some peaks around 2.2 GHz that the simulations are not being able to reproduce and, therefore it comes from another non-linear constant not considered yet.

In the previous characterization subsection, the nonlinear constants of the reflector section were not considered. Fig. 13 right depicts the IMD3 response when apart from the previous $c_{3,MR}^E$ and $c_{3,NMR}$ nonlinear constants of the IDT section, its corresponding counterpart of the reflector section $c_{3,MRr}^E$, $c_{3,NMRr}$ are activated. As evidenced in Fig. 13 right, some peaks

appear now around 2.2 GHz so it seems that those peaks on the IMD3 come from the reflectors.

Note also that the measured out-of-band IMD3 at lower frequencies unveils than an additional nonlinear term should be included to increase the IMD3 since the terms $c_{3,MR}^E$ and $c_{3,NMR}$ clearly underestimate the IMD3. At a first glance this out-of-band IMD3 could be adjusted using a nonlinear term that accompanies the electric field into the constitutive equations, such as, $e_{3,MR}^E$ or $\varepsilon_{3,MR}^S$. However, we checked with additional experiments that the slope of the IMD3 at those frequencies does not follow the characteristic slope 3 as a function of the input power, even at moderate input power levels, at which saturation effects are not expected. Therefore, we are not confident that those terms are the responsible of the measured out-of-band IMD3 and further investigation must be done.
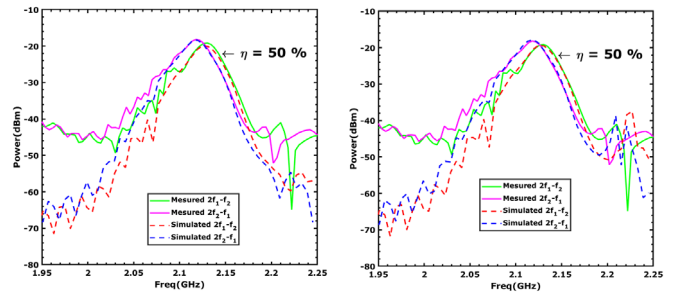

Fig. 13. IMD3 response of reference resonator with *η=50%*. Left shows simulations only considering nonlinear coefficient of the IDT area. Contrarily, right shows simulations adding the reflector nonlinear coefficients.

D. Characterization process validation

Once identified the potential contributors of the IMD3 nonlinear response of the reference resonator, the characterization process is validated testing the same nonlinear parameters $c_{3,MR}^E = c_{3,MRr}^E = c_{3,NMR} = c_{3,NMRr} = -110c^E$ in both Set 1 and Set 2 resonators. Fig. 14 shows the IMD3 response of the Set 1 resonators. As it can be seen, the proposed nonlinear parameters are consistent for all the resonators with different duty factor for the in-band IMD3 prediction.

Fig. 15 shows the results for the Set 2 resonators. Again, the tested values are consistent with the measurements.
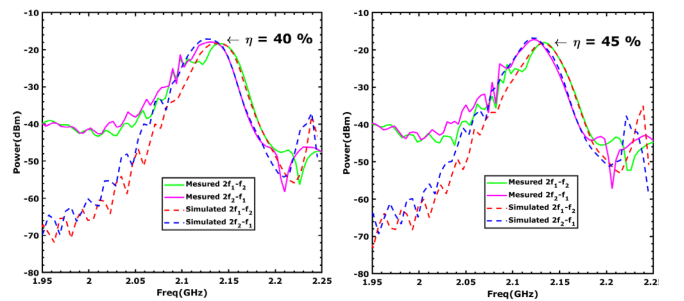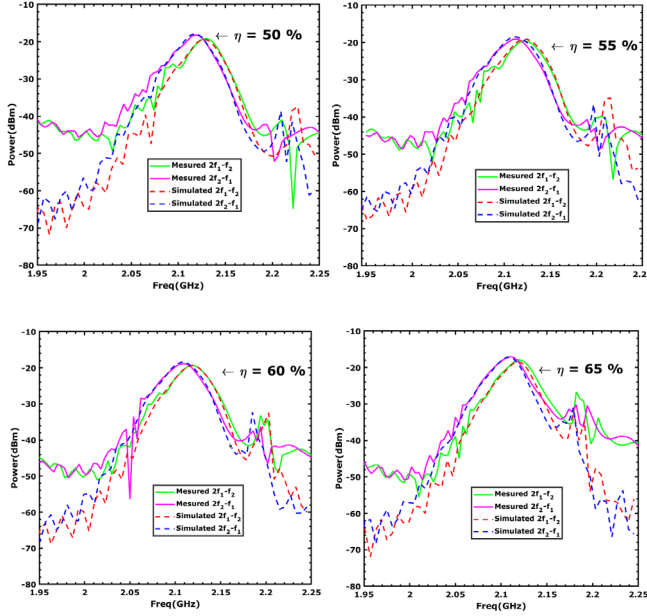
Fig. 14. IMD3 response of Set 1 SAW resonators. Red and blue dashed traces correspond to simulated *2f₁-f₂* and *2f₂-f₁* respectively, and measured responses in green (*2f₁-f₂*) and magenta (*2f₂-f₁*) traces.
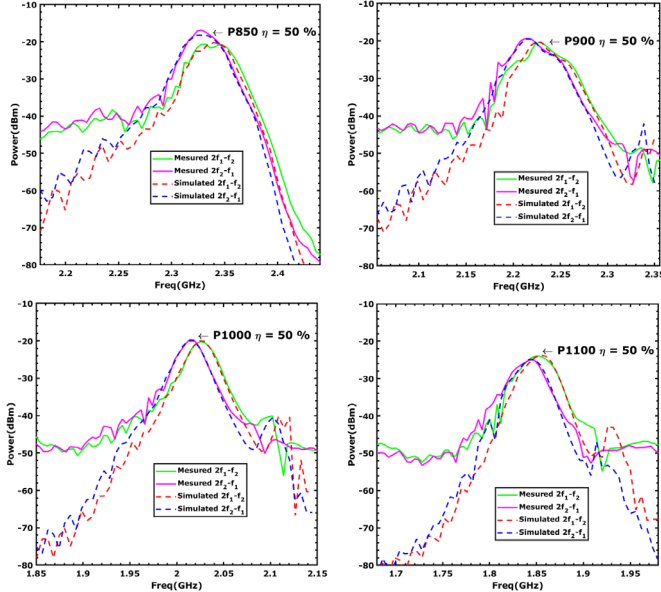

Fig. 15. IMD3 response of Set 2 SAW resonators. Red and blue dashed traces correspond to simulated *2f₁-f₂* and *2f₂-f₁* respectively, and measured responses in green (*2f₁-f₂*) and magenta (*2f₂-f₁*) traces.

Note that although simulations show very good results for both Set 1 and Set 2 in the in-band IMD3 frequency response, there are still some discrepancies between simulations and measurements at lower and higher frequencies as commented previously and further investigation would be needed for modelling the out-of-band IMD3.

Note that the value of $c_{3,MR}^E$ we got form the experiments, must be considered as an effective value for a given stack of layers and materials (and cut-orientation) along the thickness direction and not as an intrinsic parameter of any material composing the stack, since the standing wave along the thickness direction of the propagating mode is not considered.

V. CONCLUSION

The proposed application of the IOES method has demonstrated to be extremely useful for the analysis of large distributed nonlinear circuits, as it is the case of SAW resonators. Considering a simple structure composed by 5 λ-sections in both IDT and reflector regions with 400 nonlinear unitary cells per λ-section and 51 frequency points the IOES method is 1000 times faster than a commercial software using HB. For more λ-sections the improvement is drastically enhanced since the computing time of the proposed method does not increase exponentially with the problem size, in fact, the improvement is enhanced with more sections. For example, the computing time required by the analysis of a resonator with 100 and 20 λ-sections for the active region and each reflector respectively, is less than 35.4 s (51 frequency points) while these simulations are unaffordable using HB techniques.

The distributed model of a SAW resonator described here and the IOES method has been applied to analyze the measured IMD3 of 10 resonators with different pitch and duty factor, concluding than only one shape independent parameter, the third order derivative of the elastic constant with a value of $c_{3,MR}^E = -110c^E$, can explain all the measured in-band IMD3 around resonance within an error of ±0.5 dB. Under our knowledge there is no previous works showing such degree of agreement between simulations and measurements for different in-line geometries using the same nonlinear parameter. This validates the idea that a distributed model governed by local constitutive equations is fundamental to predict the IMD3 of other resonators before manufacturing.

The distributed model described here and the IOES method is not restricted to a specific in-plane geometry and it is perfectly suitable to simulate the nonlinearities of more complex structures, such as ladder filters or coupled resonators filters.

Although the in-band IMD3 is very well predicted, the simulations we presented here by the model are unable to accurately predict the out-of-band IMD3. Despite the out-of-band IMD3 power level is smaller, it is worth making further research to include additional complexity to the circuit model, for example, bulk wave radiation, or even to apply the IOES method to other type of equivalent models, such as the P-matrix model in order to provide better simulations of the out-of-band linear response and consequently of the out-of-band IMD3.

APPENDIX I

Admittance matrices

The admittance matrix of a section of transmission line (Fig. A.1 left), is

$$\frac{1}{z_s(2z_p + z_s)}\begin{bmatrix} z_p + z_s & -z_p \\ -z_p & z_p + z_s \end{bmatrix} \tag{32}$$

and the one of the 4-port MR section (Fig A.1 right) is

$$\begin{bmatrix} \left(1+\frac{z_{p'}}{z_{s'}}\right)\frac{1}{D} & \left(\frac{-z_{p'}}{z_{s'}}\right)\frac{1}{D} & \frac{T}{D} & -\frac{T}{D} \\ \left(\frac{-z_{p'}}{z_{s'}}\right)\frac{1}{D} & \left(1+\frac{z_{p'}}{z_{s'}}\right)\frac{1}{D} & \frac{T}{D} & -\frac{T}{D} \\ \frac{T}{D} & \frac{T}{D} & \frac{2T^2+j\omega C_o(2z_{p'}+z_{s'})}{D} & -\left(\frac{2T^2+j\omega C_o(2z_{p'}+z_{s'})}{D}\right) \\ -\frac{T}{D} & -\frac{T}{D} & -\left(\frac{2T^2+j\omega C_o(2z_{p'}+z_{s'})}{D}\right) & \frac{2T^2+j\omega C_o(2z_{p'}+z_{s'})}{D} \end{bmatrix} \quad (33)$$
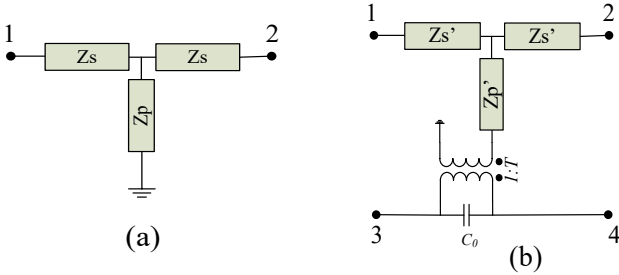
with $D = \left(2Z_{p'} + Z_{s'}\right)$.

Fig. A.1 (a) Schematic section of T-network (NMR). (b) 4-Port Crossed-field network (MR).

The admittance matrix of a λ-section is formed by 7 nodes as depicted in Fig. 4(b). Basically, this matrix is made up by connecting the admittance matrix of each MR and NMR corresponding with Fig. A.1(a) and Fig. A.1(b) respectively. Since the MR and NMR are formed by 2 and 4 ports respectively, the final admittance matrix of the λ-section is built up by joining the common nodes corresponding to the top nodes acoustically and the bottom nodes electrically. Moreover, the electrical part accounts for the polarization of the electrodes and one node for each MR is grounded (see Fig. 4 (b)), resulting in a final matrix of $[\mathbf{Y}_\omega]_{7x7}$.

APPENDIX II

Standing wave patterns at targeted frequency for remix purposes (metallized region)

To illustrate the required steps to evaluate the remix effects, let us assume we want to calculate the H3 generated by remix effects. Then, we will need to find the standing wave pattern at the frequency H2, which cannot be done as it was done before for the fundamental signals since the nonlinear sources at H2 are distributed along the section.

Once the circuit is evaluated for H2, we know the input and output voltages $V_{1,2\omega 1}$, $V_{3,2\omega 1}$ and $V_{2,2\omega 1}$, $V_{4,2\omega 1}$ (left-side and right-side voltages of the 4-port network respectively) and its corresponding currents are calculated using the 4-ABCD matrix of the metallized region at the frequency H2:

$$I_1 = Y_{11} \cdot V_1 + Y_{12} \cdot V_2 + Y_{13} \cdot V_3 + Y_{14} \cdot V_4 - I_{eq1}, \quad (34)$$
$$I_3 = Y_{31} \cdot V_1 + Y_{32} \cdot V_2 + Y_{33} \cdot V_3 + Y_{34} \cdot V_4 - I_{eq3}, \quad (35)$$

where I_{eq1} and I_{eq3} are the input equivalent sources at H2 that were previously calculated.

Now we can apply equation (31) to find the next vector V_2, I_2, V_4, I_4 at each unit-cell, and repeat this procedure along the section. Finally, we obtain S(z) and E(z) as:

$$S(z) = -\frac{Z_p}{A_L c^E}\left(I_1(z) - I_2(z)\right) \quad (36)$$

$$E(z) = \frac{1}{d}V_3(z) \quad (37)$$

A similar procedure is followed to find the IMD3 due to remix effects. The main difference is, for example, that the remix effect of the IMD3 $2f_1$-f_2 might come from the mix of H2 at $2f_1$ with f_2 and from the mix of the IMD2 f_2-f_1 with f_1. Therefore, the magnitude distributions at $2f_1$ and at f_2-f_1 must be calculated.

APPENDIX III

A. IOES equivalent sources NMR section

Following the same mathematical procedure as explained in section III.D-1, it is possible to expand (26) cascading N identical cells as in Fig. A.2 obtaining the corresponding input current and voltage following:

$$\begin{bmatrix} V_1 \\ I_1 \end{bmatrix} = [ABCD]_{\Delta z}^N \begin{bmatrix} V_{N+1} \\ I_{N+1} \end{bmatrix} + \\ \left([ABCD]_{\Delta z}^{N-1} T_{NL,N} + \right. \\ \left. [ABCD]_{\Delta z}^{N-2} T_{NL,N-1} + \dots + T_{NL,1} I_2\right)[EF]_{\Delta z} \quad (38)$$

where $[EF]_{\Delta z}$ is a column vector having the coefficients (named E and F) corresponding to the terms multiplying $T_{NL}(z_i)$ in equation (25) and we are considering that $T_{NL}(z_i) = T_{NL,i}$ and I_2 refers to the 2x2 identity matrix. Considering that we can rewrite last equation as:

$$\begin{bmatrix} V_1 \\ I_1 \end{bmatrix} = [ABCD]_{\Delta z}^N \begin{bmatrix} V_{N+1} \\ I_{N+1} \end{bmatrix} + \begin{bmatrix} V_{eq} \\ I_{eq} \end{bmatrix} \quad (39)$$

where

$$\begin{bmatrix} V_{eq} \\ I_{eq} \end{bmatrix} \\ = \left([ABCD]_{\Delta z}^{N-1} T_{NL,N} \right. \\ \left. + [ABCD]_{\Delta z}^{N-2} T_{NL,N-1} + \dots + T_{NL,1} I_2\right)[EF]_{\Delta z} \quad (40)$$

Note that when we calculate the equivalent sources of (40), the powers of the ABCD matrix are not calculated by multiplying matrices but directly calculated changing the length of the TL as for example $[ABCD]_{\Delta z}^{N-1} = [ABCD]_{(N-1)\cdot\Delta z}$, that is using $L_m = (N-1)\cdot\Delta z$ in (1), (2), which significantly reduces the computing time.

Moreover, we use a matrix operation to calculate these equivalent sources of (40). In the case of the NMR section, this matrix operation is as follows:

$$\begin{bmatrix} V_{eq} \\ I_{eq} \end{bmatrix} = \begin{bmatrix} 1 & A_1 & \cdots A_{N-1} & 0 & B_1 & \cdots B_{N-1} \\ 0 & C_1 & \cdots C_{N-1} & 1 & D_1 & \cdots D_{N-1} \end{bmatrix} \begin{bmatrix} E\cdot T_{NL,1} \\ \vdots \\ E\cdot T_{NL,N-1} \\ E\cdot T_{NL,N} \\ F\cdot T_{NL,1} \\ \vdots \\ F\cdot T_{NL,N-1} \\ F\cdot T_{NL,N} \end{bmatrix} \quad (41)$$

where the parameters A_i, B_i, C_i, D_i are calculated accordingly to their subscript that indicates the length $i\cdot\Delta z$, where $i=1\dots N$. A similar matrix operation can be found for the MR section.

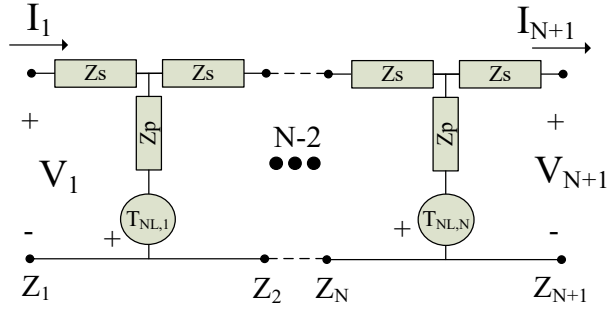Fig. A.2. V-I definition for the ABCD matrix description of non-metallized region. Example of connection of N unit-cells.
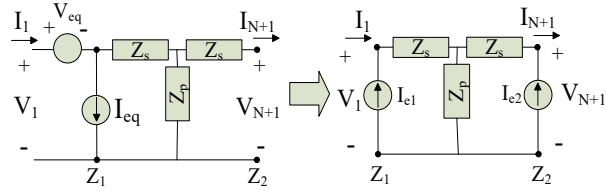

Fig. A.3. Equivalent sources of a non-metallized region.

As shown in the equations, the ABCD matrix associates the input and output current and voltages of the whole section. Moreover, it is necessary to use and additional current and voltage source following (39) to find the input-output equivalent sources I_{e1} and I_{e2} of an NMR section as shown in Fig. A.3, being the circuit of Fig. A.3 left completely equivalent to the circuit in Fig. A.3 right if the relations between equivalent sources are as follows

$$I_{e1} = \frac{1}{z_s + 2z_p}\left(1 + \frac{z_p}{z_s}\right)V_{eq} - I_{eq}$$

$$I_{e2} = \frac{-1}{z_s + 2z_p}\left(\frac{z_p}{z_s}\right)V_{eq} \tag{42}$$

where z_s and z_p correspond to the whole section of length $N \cdot \Delta z$.
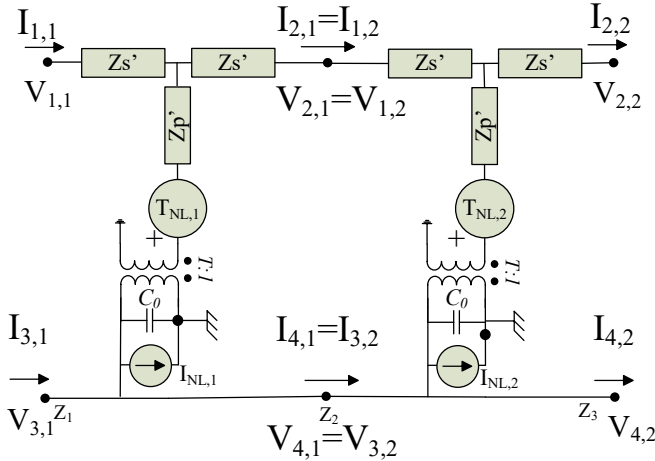

Fig. A.4. I-V definition of cascading 4-ABCD matrices of a MR section.

B. IOES equivalent sources MR section

As it was done for the NMR sections, we will use (43) as a result of the circuital analysis of the Crossed-field Mason model

of Fig. A.4. This equation relates the input and output voltages and currents to define a so-called 4-port ABCD matrix:

$$\begin{bmatrix} V_{1,i} \\ I_{1,i} \\ V_{3,i} \\ I_{3,i} \end{bmatrix} = \begin{bmatrix} \frac{z_{s'}}{z_{p'}} + 1 & \frac{z^2_{s'}}{z_{p'}} + 2z_{s'} & \frac{z_{s'}T}{z_{p'}} & 0 \\ \frac{1}{z_{p'}} & \frac{z_{s'}}{z_{p'}} + 1 & \frac{T}{z_{p'}} & 0 \\ 0 & 0 & 1 & 0 \\ \frac{T}{z_{p'}} & \frac{z_{s'}T}{z_{p'}} & \frac{T^2}{z_{p'}} + j\omega C_0 & 1 \end{bmatrix}\begin{bmatrix} V_{2,i} \\ I_{2,i} \\ V_{4,i} \\ I_{4,i} \end{bmatrix} + \begin{bmatrix} -\frac{z_{s'}}{z_{p'}} \\ \frac{1}{z_{p'}} \\ 0 \\ -\frac{T}{z_{p'}} \end{bmatrix} T_{NL}(z_i)$$
$$+ \begin{bmatrix} 0 \\ 0 \\ 0 \\ 1 \end{bmatrix} I_{NL}(z_i) \tag{43}$$

And we can rewrite (43) considering many unit cells as in Fig. A.4 following:

$$\begin{bmatrix} V_{1,1} \\ I_{1,1} \\ V_{3,1} \\ I_{3,1} \end{bmatrix} = [4ABCD]^N_{\Delta z} \cdot \begin{bmatrix} V_{2,N+1} \\ I_{2,N+1} \\ V_{4,N+1} \\ I_{4,N+1} \end{bmatrix} + \left([4ABCD]^{N-1}_{\Delta z} \cdot T_{NL,N} + [4ABCD]^{N-2}_{\Delta z} \cdot T_{NL,N-1} + \cdots + \right.$$

$$\left. T_{NL,1}I_4\right) \cdot [EFGH]_{\Delta z} + \left(\sum_{i=1}^N I_{NL,i}\right)\begin{bmatrix} 0 \\ 0 \\ 0 \\ 1 \end{bmatrix} \tag{44}$$

where $[4ABCD]^N_{\Delta z}$ is the lineal 4-port ABCD matrix of a differential Δz section of the N λ-sections, and the right terms are added terms that influence the equation of $V_{1,1}$, $I_{1,1}$, $V_{3,1}$, $I_{3,1}$ depending on the nonlinear sources $T_{NL,i}$ and $I_{NL,i}$. Note that $[EFGH]_{\Delta z}$ corresponds to the column vector multiplying $T_{NL}(z_i)$ in equation (43), and I_4 refers to the 4x4 identity matrix. If we reformulate the equation (44) we obtain:

$$\begin{bmatrix} V_{1,1} \\ I_{1,1} \\ V_{3,1} \\ I_{3,1} \end{bmatrix} = [4ABCD]^N_{\Delta z}\begin{bmatrix} V_{2,N+1} \\ I_{2,N+1} \\ V_{4,N+1} \\ I_{4,N+1} \end{bmatrix} + \begin{bmatrix} V_{1,eq} \\ I_{1,eq} \\ 0 \\ I_{3,eq} \end{bmatrix}, \tag{45}$$

Being:

$$\begin{bmatrix} V_{1,eq} \\ I_{1,eq} \\ 0 \\ I_{3,eq} \end{bmatrix} = \left([4ABCD]^{N-1}_{\Delta z} \cdot T_{NL,N} + [4ABCD]^{N-2}_{\Delta z} \cdot T_{NL,N-1} + \cdots + T_{NL,1}I_4\right) \cdot$$

$$[EFGH]_{\Delta z} + \left(\sum_{i=1}^N I_{NL,i}\right)\begin{bmatrix} 0 \\ 0 \\ 0 \\ 1 \end{bmatrix} \tag{46}$$

REFERENCES

[1] Y. Yong and X. Pang, "Nonlinear frequency response of second harmonic generation in SAW IDT resonators," in *Proc. IEEE Int. Ultrason. Symp.*, Washington, DC, Oct. 2017, pp. 1-4.

[2] L. Chen *et al*., "Third order nonlinear distortion of SAW duplexers in UMTS system," in *Proc. IEEE Int. Ultrason. Symp.*, San Diego, CA, Oct. 2010, pp. 283–286.

[3] L. Chen *et al*., "A nonlinear mason model for 3rd order harmonic and intermodulation simulations of SAW duplexers," in *Proc. IEEE Int. Ultrason. Symp.*, Dresden, Germany, Oct. 2012, pp. 56–60.

[4] S. Inoue *et al*., "A nonlinear elastic model for predicting triple beat in SAW duplexers," in *Proc. IEEE Int. Ultrason. Symp.*, Orlando, FL, Oct. 2011, pp. 1837–1841.

[5] R. Nakagawa *et al*., "Study on generation mechanisms of third-order nonlinearity in SAW devices," in *Proc. IEEE Int. Ultrason. Symp.*, Taipei, Oct. 2015, pp. 1-4.

[6] R. Nakagawa *et al*., "Discussion about generation mechanisms of third-order nonlinear signals in surface acoustic wave resonators based on simulation," *Jap. J. of App. Physics*, 2016, vol. 55, no 7S1, p. 07KD02.

[7] R. Nakagawa *et al*., "A new simulation method for nonlinear characteristics of SAW devices," in *European Microwave Integrated Circuit Conference*, Nuremberg, 2013, pp. 292-295.

[8]   M. Mayer *et al*., "Rigorous COM and P-matrix approaches to the simulation of third-order intermodulation distortion and triple beat in SAW filters," in *Proc. IEEE Int. Ultrason. Symp.,* Prague, Jul. 2013, pp. 1965–1968.

[9]   V. Chauhan *et al*., "A P-Matrix Model for Third Order Electric and Acoustic Nonlinearities in TC-SAW Devices," in *Proc. IEEE Int. Ultrason. Symp.*, Kobe, Japan, 2018, pp. 1-4.

[10] M. Mayer *et al*., "Application of a rigorous nonlinear P-matrix method to the simulation of third order intermodulation in test devices and duplexers," in *Proc. IEEE Int. Ultrason. Symp*. Chicago, IL, 2014, pp. 787-790.

[11] M. Solal, L. Chen, J. Gratier, and S. Hester, "A nonlinear P-matrix model to simulate intermodulation products in SAW devices," in *Proc. IEEE Int. Ultrason. Symp.,* Dresden, Germany, Oct 2012, pp. 61-66.

[12] R. Nakagawa and K. Hashimoto, "Influence of electrode width of interdigital transducer on third-order nonlinearity of surface acoustic wave devices on 42° YX-LiTaO3 substrate," *Japanese Journal of Applied Physics*, 2018, vol. 57, no 7S1, pp. 07LD18.

[13] S. Inoue *et al*., "A precise nonlinear simulation for SAW duplexers considering nonlinear elasticity," in *Proc. IEEE 41st Eur. Microw. Conf.*, Manchester, Oct. 2011, pp. 599–602.

[14] S. Inoue *et al*., "Visualization of nonlinear SAW displacements in resonators induced by nonlinear elasticity," in *Proc. IEEE Int. Ultrason. Symp.*, Dresden, 2012, pp. 48-51.

[15] M. Solal, K. Kokkonen, S. Inoue, J. Briot, B. P. Abbott and K. J. Gamble, "Observation of Nonlinear Harmonic Generation of Bulk Modes in SAW Devices," *IEEE Trans. Ultrason., Ferroelectr., Freq. Control,* vol. 64, no. 9, pp. 1361-1367, Sept. 2017.

[16] X. Pang and Y. Yong, "Simulation of Nonlinear Resonance, Amplitude–Frequency, and Harmonic Generation Effects in SAW and BAW Devices," *IEEE Trans. Ultrason., Ferroelectr., Freq. Control*, vol. 67, no. 2, pp. 422-430, Feb. 2020.

[17] X. Pang and Y. Yong, "Characteristics of BAW Modes Harmonically Generated (f-2f-3f) in LiNO3 SAW Devices," in *Joint Conference of the IEEE Int. Frequency Control Symposium and European Frequency and Time Forum (EFTF/IFC)*, Orlando, FL, USA, 2019, pp. 1-2.

[18] R. Nakagawa *et al*., "Influence of electrode structure on generation of third-order nonlinearity in surface acoustic wave devices," *Japanese Journal of Applied Physics*, 2015, vol. 54, no 7S1, p. 07HD11.

[19] D. S. Shim and D. A. Feld, "A general nonlinear Mason model of arbitrary nonlinearities in a piezoelectric film," in *Proc. IEEE Int. Ultrason. Symp.*, San Diego, CA, 2010, pp. 295-300.

[20] D. A. Feld and D. S. Shim, "Determination of the nonlinear physical constants in a piezoelectric AlN film," in *Proc. IEEE Int. Ultrason. Symp.*, San Diego, CA, 2010, pp. 277-282.

[21] E. Rocas, C. Collado, J. Mateu, N. D. Orloff, J. C. Booth and R. Aigner, "Electro-thermo-mechanical Model for Bulk Acoustic Wave Resonators," *IEEE Trans. Ultrason., Ferroelectr., Freq. Control,* vol. 60, no. 11, pp. 2389-2403, November 2013.

[22] R. Perea-Robles, D. García-Pastor, J. Mateu, C. Collado and R. Aigner, "Fast Procedure for the Nonlinear Analysis of BAW Resonators," in *Proc. IEEE Int. Ultras. Symp.*, Kobe, Oct.2018, pp. 1-4.

[23] C. Collado, J. Mateu, D. Garcia-Pastor, R. Perea-Robles, A. Hueltes and R. Aigner, "Nonlinear Effects of SiO2 Layers in Bulk Acoustic Wave Resonators," *IEEE Trans. Microw. Theory Techn.,* vol. 66, no. 4, pp. 1773-1779, April 2018.

[24] D. Garcia-Pastor, C. Collado, J. Mateu and R. Aigner, "Third-Harmonic and Intermodulation Distortion in Bulk Acoustic-Wave Resonators," *IEEE Trans. Microw. Theory Techn.,* vol. 68, no. 4, pp. 1304-1311, April 2020.

[25] C. Collado, M. González-Rodríguez, J. Mateu, R. Perea-Robles and R. Aigner, "The Input-Output Equivalent Sources Method for Fast Simulations of Distributed Nonlinearities in Bulk Acoustic Wave Resonators and Filters," *IEEE Trans. Ultrason., Ferroelectr., Freq. Control,* vol. 68, no. 511, pp. 1907-1918, December 2020.

[26] M. González-Rodríguez, C. Collado, J. Mateu, J. M. Gonzalez-Arbesú, S. Huebner and R. Aigner, "Fast simulation method of Distributed Nonlinearities in Surface Acoustic Wave Resonators," *2020 IEEE Int. Ultrasonics Symposium (IUS)*, Las Vegas, NV, USA, 2020, pp. 1-4.

[27] D.Royer and E. Dieulesaint, "Piezoelectric Transducers for Bulk Waves," in *Elastic Waves in Solids,* 2nd ed., vol. 2, S. N. Lyle, Springer, Germany, 2000, pp. 6–15.

[28] Smith, W. Richard, *et al*., "Analysis of interdigital surface wave transducers by use of an equivalent circuit model," *IEEE Trans. Microw. Theory Techn.,* vol. 17, no. 11, pp. 856-864, November 1969.

[29] D.Royer and E. Dieulesaint, Interdigital-Electrode Transducers for Surface Waves," in *Elastic Waves in Solids,* 2nd ed., vol. 2, S. N. Lyle, Springer, Germany, 2000, pp. 139–143.

[30] L. Chen, M. Solal, J. Briot, S. Hester, D. Malocha and P. Wahid, "A nonlinear mason model for 3rd order harmonic and intermodulation simulations of SAW duplexers," *2012 IEEE International Ultrasonics Symposium*, 2012, pp. 56-60, doi: 10.1109/ULTSYM.2012.0015.

[31] B. A. Auld, *Acoustic Fields and Waves in Solids*, vol. 1, Malabar, FL: Krieger, 1990

[32] D. M. Pozar, *Microwave engineering*, 4th ed, John Wiley & Sons, Hoboken, NJ, 2011.

[33] J.C. Pedro, N. B. Carvalho, *Intermodulation Distortion in Microwave and Wireless Circuits*, Artech House, 2003. ISBN 1-58053-356-6.

[34] R. Nakagawa *et al*., "Study on generation mechanisms of second-order nonlinear signals in surface acoustic wave devices and their suppression," *Japanese Journal of Applied Physics*, 2015, vol. 54, no 7S1, p. 07HD12.

[35] M. Ueda, *et al*., "Nonlinear distortion of acoustic devices for radio-frequency front-end circuit and its suppression," *Japanese Journal of Applied Physics*, 2010, vol. 49, no 7S, p. 07HD12.

[36] Advanced Design System, Keysight Technologies, Santa Rosa, CA, Jan. 2016.

[37] MATLAB. 9.5.0.1298439 (R2018b). Natick, Massachusetts: The MathWorks Inc.; 2018.

[38] K. Hashimoto *et al*., "Effects of bulk wave radiation on IDT admittance on 42ºYX-LiTaO₃," in *IEEE Trans. Ultrason., Ferroelectr., Freq. Control,* vol. 48, no. 5, pp. 1419-1425, September 2001.